






Magnetic ground state and strain-mediated chiral-like atomic distortion behavior in a two-dimensional rectangular spin lattice

Yu Liao ^{1,*}, Yueqiao Qu ^{2,*}, Zuo Li ¹, Yu Chen,³ Liang Liu,⁴ Jun-Zhong Wang ^{1,†} and Gang Yao ^{1,‡}

¹Chongqing key Laboratory of Micro & Nano Structure Optoelectronics, School of Physical Science and Technology, Southwest University, Chongqing 400715, China

²Key Laboratory of Artificial Structures and Quantum Control (Ministry of Education), School of Physics and Astronomy, Shanghai Jiao Tong University, Shanghai 200240, China

³School of Science, Inner Mongolia University of Technology, Hohhot 010051, China

⁴School of Physics, State Key Laboratory for Crystal Materials, Shandong University, Jinan 250100, China



(Received 26 May 2024; revised 12 July 2024; accepted 5 August 2024; published 28 August 2024)

Due to the large perpendicular magnetic anisotropy originating from spin-orbit coupling, magnetoelastic coupling is generally reported in easy-plane magnets with rectangular lattice where the easy axis is coupled with the lattice direction. Nevertheless, the acquisition of a coupling beyond the easy-plane ferromagnets in two-dimensional (2D) materials remains unknown. Here, by employing density functional theory calculations, we demonstrate this feasibility with the discovery of long-range ferromagnetic (FM) ordering and elastic strain-mediated chiral-like atomic distortion behavior in a newly tetragonal As-Fe-As trilayer (t-FeAs monolayer), which shows large perpendicular magnetic anisotropy, robust FM ordering, and in-plane ferroelasticity (FEL). We firstly point out that obvious limits exist when using the four magnetic configurations to determine the magnetic transition temperature for a rectangular spin lattice even if more exchange interaction parameters are included. A four-state mapping analysis is carefully examined for t-FeAs, where the calculated Curie temperature T_c is 435 K, which is higher than most reported 2D magnets and can be further tuned by appropriate strains. Intriguingly, the chiral-like atomic distortion behavior of the Fe sublayer is scanning-tunneling-microscopy characterizable, which can switch the magnetization axis between the out-of-plane and in-plane directions. This unusual finding of FEL manipulation of both the atomic displacement and spin properties makes t-FeAs a promising candidate for future spintronics and provides the possibility for exploring unprecedented coupling physics.

DOI: [10.1103/PhysRevB.110.085432](https://doi.org/10.1103/PhysRevB.110.085432)

I. INTRODUCTION

Since the discovery of nanometer-scale graphene, two-dimensional (2D) magnetic materials with high tunable physical properties have attracted research interest [1–5]. Multiferroicity—an intriguing physical property arising from the combination of > 2 ferroic orders among ferromagnetism (FM), ferroelasticity (FEL), ferroelectricity, and ferrotoidicity—holds great potential for multiple-state memory, switches, and computing [6–9]. As an example, a magneto-electric material allows for the control of magnetism (electric polarization) by external electric field (magnetic field). Comparatively, FM-FEL materials allow the operation through the mode of writing mechanically and reading magnetically and promise an extension of the spectrum of applications for multiferroic materials. This material is particularly advantageous, as it opens the door for realizing the combination of nonvolatile memory and FM in a single-material circuit. However, ferroelectricity commonly necessitates vacant d/f

orbitals, whereas FM is often linked to partially filled d/f orbitals. The conflicting origins of these ferroic orders makes the inherent magneto-electric materials very scarce. Although FEL has been experimentally demonstrated or theoretically predicted in 2D systems, such as layered-perovskite thin films, transition metal dichalcogenides, phosphorene and phosphorene analogs as well as honeycomb lattices (including graphene, BN, and stanene) [10–16], their nonmagnetic nature greatly restricts their applications in spintronics. To this end, 2D FEL lattices with desirable magnetic and mechanical properties for scalable spintronic device applications are in urgent need.

The absence of magnetism in many 2D materials has motivated great efforts to artificially introduce or control spin ordering via doping [17,18], defect engineering [19,20], and proximity coupling [21,22]. Typically, arising from the van Hove singularity of valence band edges, FM is derived in nonmagnetic but FEL monolayers of α -SnO and α -PbO under carrier doping [17,18]. So far, plenty of 2D materials with coexisting FEL and intrinsic FM characters have also been reported [23–28], but few of them possess both high-temperature magnetism and observable FEL switching signals. There are even fewer materials that exhibit coupling between these two orders, which have severely

*These authors contributed equally to this work.

†Contact author: jzwangcn@swu.edu.cn

‡Contact author: yaogang@swu.edu.cn

hampered their applications for functional devices. For instance, in 2D ferromagnets with rectangular lattices, FEL is inherent. This category of materials therefore distinguishes itself among 2D crystals and could potentially serve as the highly desired monolayer magnetic component which is essential for creating comprehensive spintronic devices, offering the additional benefit of enabling FEL adjustment of the magnetic state. Nevertheless, creating 2D FM/FEL crystals possessing room-temperature intrinsic FM, low-FEL barriers, strong switching signals, and importantly, the cross-coupling between these orders remains imperative and exceedingly arduous.

Here, via first-principles calculations, molecular dynamics, and Monte Carlo (MC) simulations, we unveil that monolayer tetragonal FeAs (t-FeAs) with a rectangular lattice, a phase of the reported 2D FeAs family, exhibits an interesting coexistence of FM ordering and multiferroic couplings. We estimate the critical temperature for the magnetic transition T_c and suggest that mechanical strains can switch the T_c . Owing to the inherent crystal anisotropy, t-FeAs exhibits a FEL switching with moderate barrier and strong transition signal, making it FM-FEL multiferroic. Furthermore, a chiral-like atomic displacement is observed, followed by magnetization switchable behavior. In this paper, we indicate that t-FeAs can be an excellent candidate for advanced device applications.

II. COMPUTATIONAL PROCEDURES

Our first-principles calculations are carried out within spin-polarized density functional theory (DFT) by using VASP [29,30]. The generalized gradient approximation (GGA) of the Perdew-Burke-Ernzerhof (PBE) [31] functional for the exchange-correlation potential is adopted. The electron-ion interactions are described using the projector-augmented wave (PAW) method [29]. The localized Fe- d orbitals are treated employing the GGA + U approach with a Hubbard $U_{\text{eff}} = U - J = 3$ eV. To ensure the decoupling between the monolayer and its periodic layer, a vacuum space of 20 Å is added along the c axis. We find it is sufficient to take a combination of cutoff energy of 500 eV for plane-wave basis expansion and a Γ -centered $15 \times 15 \times 1$ Monkhorst-Pack grid for the Brillouin zone integration to obtain the convergence which is 10^{-6} eV for the electronic self-consistency loop and 10^{-2} eV/Å for the Hellmann-Feynman forces on each atom. The magnetocrystalline anisotropy energies (MAEs) are calculated using a dense k mesh of $31 \times 31 \times 1$, and the spin-orbit coupling (SOC) effect is included. The nudged elastic band (NEB) method is also implemented to estimate the energy barriers between different phases [32]. The phonon dispersions are calculated with the finite displacement method and the PBE functional on a $3 \times 3 \times 1$ supercell using the PHONOPY code [33]. *Ab initio* molecular dynamics (AIMD) simulations are performed at 300 K using the NVT ensemble up to 10 ps with a time step of 2.5 fs. The scanning tunneling microscopy (STM) simulations are performed with the Tersoff-Hamann method at constant height mode [34]. The distance between the STM tip and the sample surface is set at 3 Å. The geometries and spin-charge densities are visualized by the VESTA package [35].

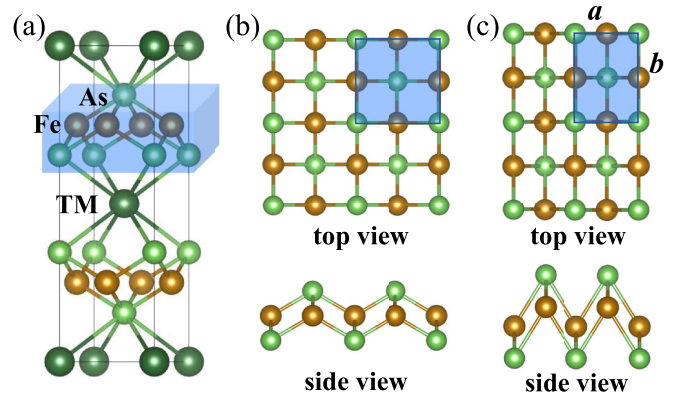


FIG. 1. Geometric structures of monolayer FeAs and its bulk counterpart. (a) Crystal structure shared by the $TMFe_2As_2$ ($TM = Ba, Ca, \text{ and } Cs$) bulk phases, where one sublayer of FeAs in its unit cell is denoted by the blue shaded cuboid. The TM , Fe, and As atoms are displayed in dark green, orange, and green, respectively. The black box shows the unit cell. (b) and (c) The top and side views of single-layer FeAs before and after optimization, respectively. The blue shaded regions denote the unit cells.

III. CRYSTAL STRUCTURE AND STABILITY OF t-FeAs

The experimentally synthesized single-crystal $TMFe_2As_2$ ($TM = Ba, Ca, \text{ and } Cs$) bulk crystallizes with space group of $I4/mmm$ and consists of alternating a As-Fe-As trilayer and a TM atom layer stacked along the c axis, as displayed in Fig. 1(a). Monolayer FeAs [Fig. 1(b)], which is the focus of this paper, has a tetragonal lattice in the $P4/nmm$ space group and is isostructural to the famous interface high-temperature superconductor of the FeSe layer [36,37]. By modeling the exfoliation process, the exfoliation energies ($0.103\text{--}0.181$ eV/Å²; see Fig. S1 in the Supplemental Material [38]) are comparable with those of MXenes and 2D non-van der Waals materials ($0.086\text{--}0.205$ eV/Å²) [39–42]. Thus, a FeAs nanosheet could be obtained from its bulk counterparts. Nevertheless, after successful optimizations, monolayer FeAs retains its tetragonal puckered form but changes from a square lattice to a rectangular one (denoted as t-FeAs), with lattice constants of $a = 2.83$ Å and $b = 3.97$ Å, and the point symmetry thus changes from C_{4v} to C_{2v} [Fig. 1(c)].

We note that our optimized lattice is considerably similar to a recent proposed phase, which also hosts a rectangular cell but moderate aspect ratio ($a = 3.17$ Å and $b = 3.80$ Å), denoted as MR-FeAs [43]. The dynamical and thermal stabilities of both systems are evidenced by the phonon spectra and AIMD simulations (Fig. S2 in the Supplemental Material [38]). Additionally, three different phases of the FeAs monolayer were also predicated previously [44], including two forms of square lattices (FeAs-I and FeAs-III) and a trigonal structure one (FeAs-II). As compared in Fig. S3 in the Supplemental Material [38], our proposed 2D lattice of FeAs is only 117 meV/atom higher than that of the most stable FeAs-I phase and much lower than the remaining three phases in energy of at least 33 meV/atom, indicating its competitive chemical stability. As a key factor in theoretically designed 2D materials, the good kinetic

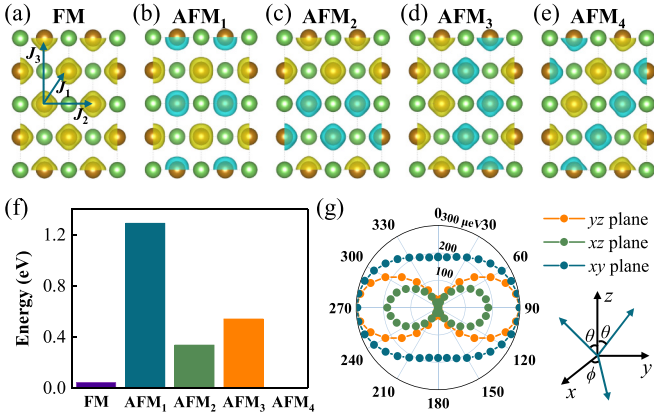


FIG. 2. Magnetic properties. (a)–(e) The isosurface plots ($0.67 \text{ e}/\text{\AA}^3$) of the spatial spin density for t-FeAs monolayer in FM and four possible AFM configurations: AFM₁, AFM₂, AFM₃, and AFM₄. The majority and minority spin charges are indicated by isosurfaces with yellow and blue colors, respectively. Blue arrows represent the exchange path of nearest-neighbor (NN), second-, and third-NN Heisenberg exchange interactions (J_1 , J_2 , and J_3). (f) Relative total energies of the various magnetic configurations shown in (a)–(e), where the total energy of AFM₄ is taken as a reference. The energies are calculated without the inclusion of SOC. (g) Angular dependence of MAE, obtained by rotating the spin orientations within xy , xz , and yz planes. The zero polar angle points along the positive z axis in the xz/yz planes, while along the x axis in the xy plane, as indicated.

stability is supported by a large positive cohesive energy (E_{coh}). For t-FeAs, $E_{\text{coh}} = (2 \times E_{\text{Fe}} + 2 \times E_{\text{As}} - E_{\text{FeAs}})/4$, where E_{Fe} , E_{As} , and E_{FeAs} are the total energies of the Fe atom, As atom, and 2D FeAs unit cell, respectively. We obtain $E_{\text{coh}} = 2.89 \text{ eV/atom}$, which is comparable with other well-known materials, such as the experimental fabricated planar hexa-coordinated Cu_2Si (3.46 eV/atom) [45] and Cu_2Ge (3.17 eV/atom) [46]. These results support the thermodynamic feasibility of synthesizing the t-FeAs monolayer in experiments.

IV. PROCEDURE TO DETERMINE THE HIGH CURIE TEMPERATURE OF t-FeAs

A. Limitations of four-spin-configurations method

After having established the structure and stability of 2D FeAs, its magnetic and electronic properties are further investigated. Generally, for a 2D magnet, one FM and several antiferromagnetic (AFM) configurations are considered to reveal the preferred spin ordering by comparing their total energies. As displayed in Figs. 2(a)–2(e), five possible magnetic configurations are adopted for t-FeAs, and their total energies are compared in Fig. 2(f). The energy of the FM configuration is found much lower than that of AFM₁, AFM₂, and AFM₃ but slightly higher than AFM₄ by $10.4 \text{ meV/unit cell}$. Due to this tiny energy difference, whether the magnetic ground state is FM or AFM cannot be precisely determined. Meanwhile, as previously reported [47], the spin-exchange interactions are also valid evidence of the magnetic ground state, which can be extracted by mapping the DFT energies to the Heisenberg

TABLE I. The spin configuration results for the Heisenberg exchange parameters extracted from Eqs. (2)–(6) without SOC and the estimated Curie temperatures (T_c) of t-FeAs.

Configurations	J_1 (meV)	J_2 (meV)	J_3 (meV)	T_c (K)
FM + AFM _{1,2,3}	−39.07	10.50	20.71	150
FM + AFM _{1,2,4}	−39.07	27.94	20.71	13
FM + AFM _{1,3,4}	−39.07	10.50	22.53	160
FM + AFM _{2,3,4}	−52.15	27.94	33.79	16

spin Hamiltonian:

$$H = \sum_{\langle i,j \rangle} J_1 \mathbf{S}_i \cdot \mathbf{S}_j + \sum_{\langle i,j \rangle} J_2 \mathbf{S}_i \cdot \mathbf{S}_j + \sum_{\langle i,j \rangle} J_3 \mathbf{S}_i \cdot \mathbf{S}_j + A (\mathbf{S}_i^z)^2, \quad (1)$$

In Eq. (1), \mathbf{S}_i (\mathbf{S}_j) is the unit vector ($S = 1$) of local spin at the i th (j th) Fe atom, A is the single-site magnetic anisotropy parameter, \mathbf{S}_i^z represents the z (i.e., out-of-plane orientation) component of \mathbf{S} , $J_{1,2,3}$ is the isotropic Heisenberg exchange coupling between two different Fe atoms at sites i and j [Fig. 2(a)], and negative (positive) J implies FM (AFM) exchange interaction. For previously reported 2D monolayers of CrSiSe_3 [47] and strained Janus Cr_2XYTe_6 ($X, Y = \text{Si, Ge, Sn}$, and $X \neq Y$) [48], an incorrect magnetic ground state had been yielded when ignoring J_2 and J_3 . It is thus necessary to study the preferred magnetic coupling by performing MC simulation with multiple exchange interactions, usually up to the third one (J_3).

For the different spin configurations [Figs. 2(a)–2(e)], the total energy can be expressed as

$$\frac{E_{\text{FM}}}{4} = E_0 + (4J_1 + 2J_2 + 2J_3)S^2 - AS^2, \quad (2)$$

$$\frac{E_{\text{AFM1}}}{4} = E_0 + (-4J_1 + 2J_2 + 2J_3)S^2 - AS^2, \quad (3)$$

$$\frac{E_{\text{AFM2}}}{4} = E_0 + (0J_1 + 2J_2 - 2J_3)S^2 - AS^2, \quad (4)$$

$$\frac{E_{\text{AFM3}}}{4} = E_0 + (0J_1 - 2J_2 + 2J_3)S^2 - AS^2, \quad (5)$$

$$\frac{E_{\text{AFM4}}}{4} = E_0 + (0J_1 - 2J_2 - 2J_3)S^2 - AS^2, \quad (6)$$

where E_0 is the total energy independent of different magnetic states. Note that we set $S = 1$, and parameter A in Eq. (1) is kept. As listed in Table I, J_1 , J_2 , and J_3 are very dependent upon the choice of spin configurations. A similar result was previously reported for a rectangular monolayer of Cr_2Te_6 [49]. By performing MC simulations based on the spin Hamiltonian parametrized with the MAEs and $J_{i,j}$ in Eq. (1), nonzero T_c are always obtained (Table I), implying FM coupling in t-FeAs. In addition, the T_c 's are significant different, with values ranging from 13 to 160 K. Therefore, it can be concluded that the four-spin-configurations method has an obvious limit in determining exchange interaction parameters and hence the magnetic transition temperature for a rectangular spin lattice.

At the end of this section, we make additional remarks to the MAE, defined as $\text{MAE} = E_{\parallel} - E_{\perp}$, where E_{\parallel} and E_{\perp} are the total energies of in-plane $M_a[100]$ and $M_b[010]$ and out-of-plane $M_c[001]$ spin configurations, respectively. According to the Mermin-Wagner theorem [50], the magnetically ordered phase of 2D materials is dependent on the MAE and the distance dependence of the exchange interaction. Also, in a 2D system, a stable long-range magnetic ordering which is robust against the thermal fluctuations is beneficial to magnetic data storage. Figure 2(g) displays the MAE as a function of polar angles on the xy , xz , and yz planes. The lowest energy state corresponds to the $M_c[001]$ direction, indicating out-of-plane magnetization. Using the total energy corresponding to the $M_c[001]$ direction as a reference, we obtain $\text{MAE}_{[100]-[001]} = 184 \mu\text{eV}/\text{Fe atom}$ and $\text{MAE}_{[010]-[001]} = 299 \mu\text{eV}/\text{Fe}$, suggesting large out-of-plane magnetic anisotropy. Therefore, t-FeAs belongs to the category of 2D Ising magnets possessing a long-range (AFM)FM ordered low-temperature phase, being the reason for the spin Hamiltonian we selected. Note that the MAE value for t-FeAs is > 3 times larger than that of cubic Ni ($2.7 \mu\text{eV}/\text{atom}$), Fe ($1.4 \mu\text{eV}/\text{atom}$), and Co ($65 \mu\text{eV}/\text{atom}$) [51,52]. The large MAE values render t-FeAs appropriate for applications in magnetoelectronics.

B. Estimate of T_c based on the four-state mapping analysis

To make the exchange parameters and hence T_c clear, a four-state mapping analysis is applied [53,54]. In this method, the J -related total energy of magnetic configuration is written as

$$E_{\text{spin}} = J_{12}\mathbf{S}_1 \cdot \mathbf{S}_2 + \mathbf{S}_1 \cdot \mathbf{K}_1 + \mathbf{S}_2 \cdot \mathbf{K}_2 + E_{\text{other}}, \quad (7)$$

where $\mathbf{K}_1 = \sum_{i \neq 1,2} J_{1i}\mathbf{S}_i$, $\mathbf{K}_2 = \sum_{i \neq 1,2} J_{2i}\mathbf{S}_i$, $E_{\text{other}} = \sum_{i \neq 1,2} J_{i,j}\mathbf{S}_i \cdot \mathbf{S}_j$, and J_{12} denotes the exchange interaction between two spins at sites 1 and 2. Four collinear spin states including (1) $\mathbf{S}_1^z = \mathbf{S}$, $\mathbf{S}_2^z = \mathbf{S}$; (2) $\mathbf{S}_1^z = \mathbf{S}$, $\mathbf{S}_2^z = -\mathbf{S}$; (3) $\mathbf{S}_1^z = -\mathbf{S}$, $\mathbf{S}_2^z = \mathbf{S}$; and (4) $\mathbf{S}_1^z = -\mathbf{S}$, $\mathbf{S}_2^z = -\mathbf{S}$ are considered. Meanwhile, the spin orientations of other spin sites are always set the same. This method is irrelevant to the spin configurations shown in Figs. 2(a)–2(e), and a more accurate J value will be extracted if a larger spin lattice is used.

Take J_3 calculation as an example. The corresponding spin states based on a $5 \times 5 \times 1$ supercell are displayed in Figs. 3(a)–3(c). The energy expressions for these four spin states are

$$E_1 = E_0 + E_{\text{other}} + J_3\mathbf{S}^2 + K_1\mathbf{S} + K_2\mathbf{S}, \quad (8)$$

$$E_2 = E_0 + E_{\text{other}} - J_3\mathbf{S}^2 + K_1\mathbf{S} - K_2\mathbf{S}, \quad (9)$$

$$E_3 = E_0 + E_{\text{other}} - J_3\mathbf{S}^2 - K_1\mathbf{S} + K_2\mathbf{S}, \quad (10)$$

$$E_4 = E_0 + E_{\text{other}} + J_3\mathbf{S}^2 - K_1\mathbf{S} - K_2\mathbf{S}, \quad (11)$$

and J_3 can be deduced from Eqs. (8)–(11):

$$J_3 = \frac{E_1 - E_2 - E_3 + E_4}{4\mathbf{S}^2}. \quad (12)$$

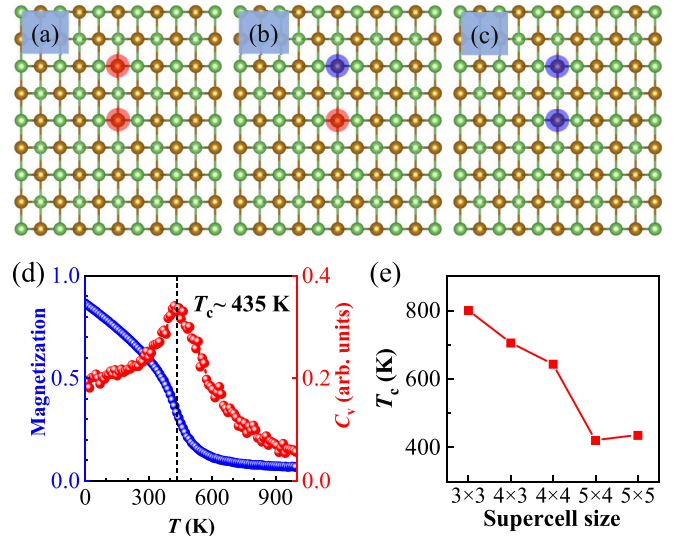


FIG. 3. Configurations with different ordered spin states and Monte Carlo (MC) simulations. (a) $\uparrow\uparrow$ spin ordering, (b) $\uparrow\downarrow$ or $\downarrow\downarrow$ spin orderings, and (c) $\downarrow\downarrow$ spin ordering for estimating J_3 . The up and down spins on the Fe atoms are denoted as red and blue shaded cycles, respectively. (d) Magnetization and specific heat C_v with respect to temperature. (e) Effect of the supercell size on T_c .

We obtain $J_1 = -44.06 \text{ meV}$, $J_2 = -16.64 \text{ meV}$, and $J_3 = 2.08 \text{ meV}$. Considering the rather small AFM J_3 , FM J_1 and J_2 contribute dominantly to the magnetism in t-FeAs. Since the Fe-As-Fe bonding angles ($\sim 60^\circ$) are close to 90° , the overall FM coupling is therefore driven by the superexchange of Fe atoms mediated through the As atom, according to the well-known Goodenough-Kanamori-Anderson rules [55–57]. Additionally, it should be emphasized that J_1 calculated from four-state mapping is close to the one of the four-spin-configurations method; however, J_2 changes from AFM to FM coupling, and J_3 is one order of magnitude smaller. This conflict may be valuable for theoretical works on 2D magnetic materials and needs further investigation.

From the simulated magnetization and specific heat curves in Fig. 3(d), the T_c of monolayer t-FeAs is found to be 435 K. The convergence of T_c is also tested with different supercell sizes, as shown in Fig. 3(e). The T_c difference between supercells of $5 \times 4 \times 1$ and $5 \times 5 \times 1$ is only 15 K. When considering neighboring exchange interactions up to J_5 , $J_4 = 1.46 \text{ meV}$ and $J_5 = 0.46 \text{ meV}$, a very close T_c (410 K, see Fig. S4 in the Supplemental Material [38]) is obtained. Therefore, the calculated $5 \times 5 \times 1$ supercell and numbers of spin-exchange interactions are enough to achieve the desired computation accuracy. For comparison, the T_c value of the intrinsic FM semiconductor CrI_3 estimated by the same method is 57 K for $U_{\text{eff}} = 0 \text{ eV}$ and 78 K for $U_{\text{eff}} = 3 \text{ eV}$ (Fig. S5 in the Supplemental Material [38]), very close to the experimental measurement ($\sim 45 \text{ K}$) [2] and previous theoretical values (35–75 K) [58,59], confirming the validity of our method.

Collectively, we demonstrated the importance of both including more exchange interaction parameters in determining the magnetic ground state and employing the four-state mapping analysis for the calculation of the T_c of 2D magnets

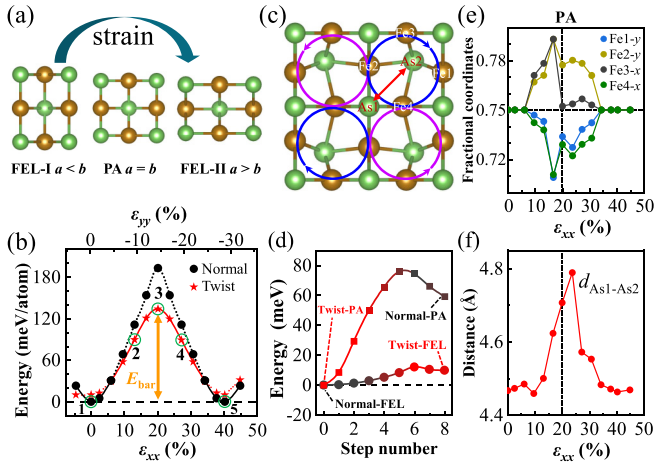


FIG. 4. In-plane ferroelasticity (FEL) of t-FeAs. (a) General FEL switching pathway of two-dimensional (2D) tetragonal materials. (b) FEL switching energy profile of t-FeAs. The energy of the initial state (FEL-I) is set to zero. (c) The optimized structure of the twist FeAs at paraelastic (PA) state, in which the deviation directions of the Fe and As atoms are indicated. (d) Changes of relative energies per atom during the phase transition between normal and twist phases for FEL-I and PA states. (e) and (f) Variations of the Fe-displacements and As-As distance with the FEL strain, indicated by the circles and red arrow in (c).

with rectangular spin lattice. The underlying mechanism of FM can be disclosed in more detail from its electronic structures. The calculated electronic band structure reveals that the t-FeAs monolayer is a spin-polarized metal (Fig. S6(a) in the Supplemental Material [38]). From the spin charge density plotted in Fig. 2(a), the major magnetism of t-FeAs is contributed by spin-polarized $3d$ orbitals of Fe atoms. The total spin magnetic moment is $\sim 3.0 \mu_B$ per Fe atom, indicating a large spin polarization in this 2D crystal. Further, the local magnetic moment on Fe and As atoms are ~ 3.048 and $-0.058 \mu_B$, respectively. Based on the charge transfer and crystal field theory, the local magnetic moment of Fe can be understood. Because of the tetrahedron crystal field of Fe atoms, the d orbitals split into a set of upper triple-degenerated t_{2g} (d_{xy}, d_{yz}, d_{xz}) and lower double-degenerated e_g ($d_{x^2-y^2}, d_z^2$), which further split into five nondegenerate orbitals, as schemed in Fig. S6(b) in the Supplemental Material [38], consistent with the calculated orbital-resolved density of states (Fig. S6(c) in the Supplemental Material [38]). In the minority spin channel, all five orbitals are occupied, while only d_z^2 and d_{xz} in the majority ones are occupied and the other three orbitals empty. Thus, a net magnetic moment of $\sim 3.0 \mu_B$ is observed, agreeing with the result from our DFT calculations.

V. MULTIFERROIC COUPLINGS

A. FEL strain-induced chiral-like atomic distortion behavior

Given the rectangular lattice of t-FeAs at its ground state, the in-plane elastic switching with a nonvolatile strain is inherent. Figure 4(a) illustrates the general FEL switching pathway for a 2D tetragonal material [17,18,25], where the

structure of the initial/FEL-I state is the same as that of the final (i.e., FEL-II) one after a rotation of 90° . These two FEL states are connected by an intermediate state with a square lattice, i.e., paraelastic (PA) state. The elastic energy ΔE_{el} for t-FeAs is calculated vs strain varying ϵ_{xx} and ϵ_{yy} for lattice constants in the x and y directions, and the internal positions are fully relaxed. The energy profile from initial to final state shown in Fig. 4(b) has two degenerate minima at $\epsilon_{xx} = 0\%$ ($\epsilon_{yy} = 0\%$) and $\epsilon_{xx} = 40.3\%$ ($\epsilon_{yy} = -28.7\%$). Clearly, t-FeAs exhibits intrinsic FEL (see the black line). Therefore, a 2D t-FeAs crystal is multiferroic that hosts FM and FEL simultaneously. It should be emphasized that, in contrast with the centrosymmetric one, a noncentrosymmetric phase named the twist phase hereafter is observed at the PA state [Fig. 4(c)], which is indeed lower in energy than the centrosymmetric one. Quite interestingly, in this 2D plane, the Fe sublattice features chiral-like lattice distortions, as indicated, while the four As atoms in internal positions of $(\frac{1}{4}, \frac{1}{4}, Z)$, $(\frac{1}{4}, \frac{3}{4}, Z)$, $(\frac{3}{4}, \frac{1}{4}, Z)$, and $(\frac{3}{4}, \frac{3}{4}, Z)$ equally move toward the corner of the cell, leading to C_{2v} symmetry rather than C_{4v} . The energy- ϵ_{xx} curve for this phase is then checked. The lattice constants a and b , during this process, are fixed under a given strain, while the internal coordinates are relaxed. A similar FEL trend is observed [red line in Fig. 4(b)]. Compared with the normal phase, the twist phase possesses higher energy at the FEL-I state but is more energetically stable at the PA state by 10 and 60 meV/atom, respectively. Thus, the true FEL-PA-FEL path is t-FeAs-twist phase-t-FeAs, namely, along the solid line in Fig. 4(b). The tiny energy difference between these two phases at the FEL-I state indicates the metastable nature of the twist phase. The critical point for the twist structural phase transition occurs at about $\epsilon_{xx} = 6\%$ ($\epsilon_{yy} = -4.3\%$), which is feasible in experiment as evidenced by the stress-strain curves (Fig. S7 in the Supplemental Material [38]). It should be noted that similar results are obtained on a larger supercell.

The transition between these two phases at the FEL-I and PA states are studied by gradually moving the internal positions [Fig. 4(d)]. One can see that, although the FEL-I state of the twist phase is just a little higher in energy than that of the normal phase, there is a small energy barrier (0.44 meV per Fe atom) between them, indicating that the metastable twist phase at the FEL-I state can survive at a high temperature without transforming to the normal one. To characterize this tendency more visibly, the offsets of the internal coordinates are summarized in Figs. 4(e) and 4(f) as a function of elastic strain. Note that, when the elastic strain deviates from the PA state, the deviations on both sides are asymmetric. Importantly, in the range from $\epsilon_{xx} = 6$ to 16.6%, the deviation of the Fe atoms from their balance positions increases as elastic strain increases linearly. The large monotonically increased tendency indicates the close relationship between the atomic displacements and FEL strain, which is expected for establishing the sensor to identify the coupling between these two orders.

To further judge the feasibility and robustness of FEL in t-FeAs, the overall transition barrier (E_{bar}) associated with the FEL lattice rotation is calculated to be 134 meV/atom, lower than that of phosphorene (200 meV/atom) [11] and BP₅ (320 meV/atom) [60], but very close to that of α -MPI ($M = \text{Zr, Hf}$;

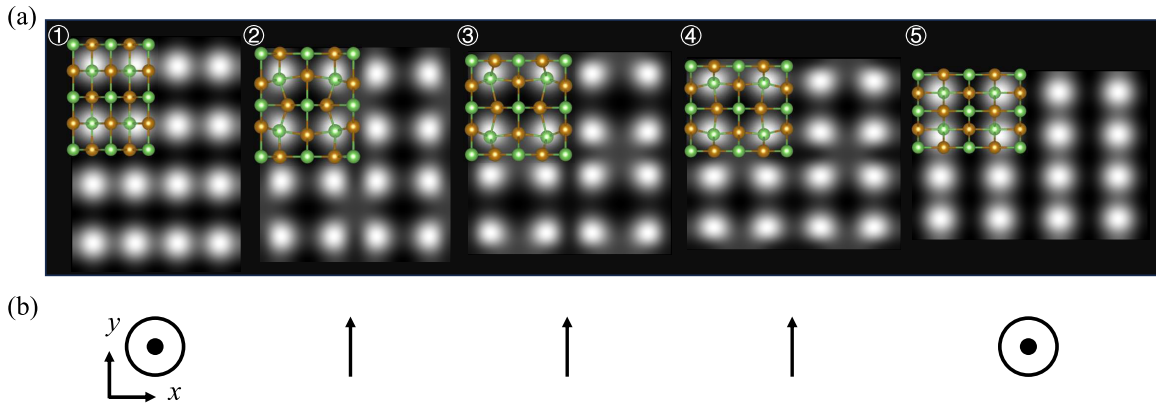


FIG. 5. Multiple multiferroic couplings. (a) The structural models and simulated scanning tunneling microscopy (STM) images of t-FeAs under various ferroelastic strains, as indicated by cycles in Fig. 4(b). The STM images are shown under a bias voltage of +0.1 V. (b) The corresponding easy axis for (a).

~ 135 meV/atom) [61]. Generally, a moderate energy barrier is desired in experiments because a small one indicates the FEL state to be unstable, while a high one makes the FEL lattice rotation hardly achieved. Therefore, the moderate value for t-FeAs renders the switchable anisotropic properties in this system upon the external stress accessible experimentally. Additionally, another key factor for FEL is the reversible strain defined as $(|b|/|a| - 1) \times 100\%$, which characterizes the structural anisotropy. The reversible FEL strain for t-FeAs is calculated to be 40.3%. Compared with previously proposed FEL materials, this value is much larger than those of VP and VAs monolayers (0.11 and 1.52%) [27] and comparable with that of phosphorene (37.9%) [11], BP₅ (41.4%) [60], and Cr-based Janus monolayers (22–36.5%) [26]. Therefore, t-FeAs would possess a strong switching signal and obvious structural anisotropic differences.

B. Coupling between atomic deviation and magnetization

It is well known that the absolute positions of atoms in the nonsurface layer are relatively difficult to measure. To obtain deeper understanding of the electronic structure and surface morphology and to aid in upcoming experimental characterization efforts, the STM images of the t-FeAs monolayer are simulated in the entire FEL switching process. Enumerated in Fig. 5(a) are a series of structural models and their corresponding simulated STM topographies of the t-FeAs monolayer as the FEL strain is gradually increased. The bright signals correspond to the topmost As atoms. Obviously, the intensity distributions of the topmost As layers of the five phases are different, indicating that the electron states in the vicinity of the Fermi level for the normal and twist phases are significantly different.

One central issue that naturally arises is whether a possible magnetoelastic coupling followed by the structural phase transition exists. In this regard, we investigate the intercoupling between the FEL strain and MAE. The detailed evaluation of MAE in the whole range of FEL switching is displayed in Fig. S8 in the Supplemental Material [38]. With small strain applied, t-FeAs retains out-of-plane magnetization. Further increasing the strain, the easy axis changes from the out-of-plane direction to the in-plane b direction at $\varepsilon_{xx} = 13.0\%$

and can be further returned to the out-of-plane one at $\sim 31\%$, leading to an interesting correlation between the easy axis and FEL strain. The tunable easy axis can be explained by the Fe- d orbitals appearing near the Fermi level, according to the second-order perturbation theory [62–64], which allows for the effective management of spin injection and detection. The preferred spin orientations corresponding to these STM images are shown in Fig. 5(b). In addition to the magnetic atomic chiral-like deviation behavior, the spin properties are also significantly linked with in-plane elastic strain, offering strong multiferroic couplings in t-FeAs. Therefore, it is possible that both the spin properties and the chiral-like atomic distortions of the Fe layer can be characterized or identified by the STM images through the changes of the intensity distribution of the surface As atoms. We expect that these features of the 2D t-FeAs monolayer provide more information for identifying the discovered chiral-like atomic distortion behavior and accelerate the possibility of its utilization in the near future.

VI. DISCUSSION

A. Tensile strain switched FM

Now in-plane tensile strain is considered to manipulate the magnetic properties in t-FeAs. Previous works indicated that MAE exhibits remarkable strain dependence in monolayer VI₃ [65], CrX₃ ($X = \text{Cl, Br, and I}$) [66], and CrWGe₂Te₆ [67]. Strain-tunable magnetism was also experimentally demonstrated at oxide domain walls [68]. Figure 6 shows the variation in T_c and MAE in t-FeAs with tensile strain. The strain can be expressed as $\varepsilon = (l - l_0)/l_0 \times 100\%$, where l_0 and l represent the lattice constants without and with strain, respectively. The strain is uniformly applied along both a and b directions or only along the a/b direction, as shown in the insets of Figs. 6(a)–6(c). Here, we consider the tensile strain up to 6%, which may be experimentally accessible, as evidenced by the stress-strain curves (Fig. S7 in the Supplemental Material [38]).

Indeed, our calculations demonstrate that the strain can easily modulate T_c . As depicted in Figs. 6(a) and 6(b), T_c decreases rapidly with increasing biaxial and uniaxial tensile strain applied along the long axial direction. Beyond $\sim 4\%$, T_c reaches zero, meaning that the magnetic behavior in t-

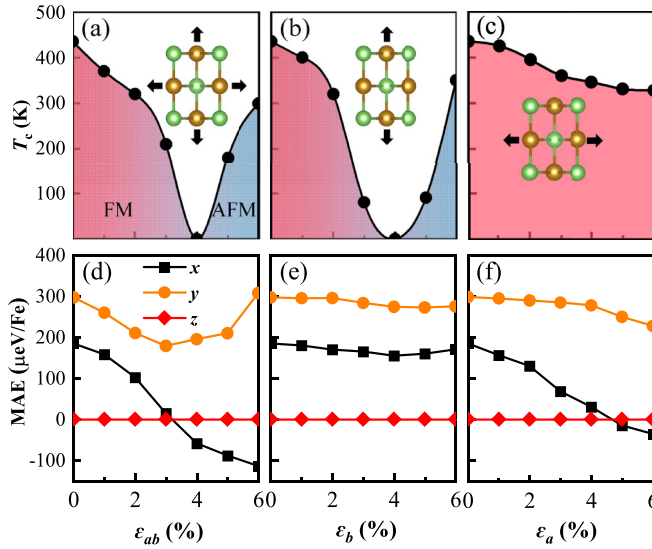


FIG. 6. Magnetic properties vs in-plane tensile strain (ϵ) in the range from 0 to 6%. (a)–(c) T_c and (d)–(f) magnetocrystalline anisotropy energy (MAE). In (d)–(f), a negative MAE implies an easy axis along the in-plane uniaxial $M_a[100]$ direction.

FeAs is transferred from FM to AFM. In contrast, the T_c 's are slightly changed in this 2D crystal under tensile strain applied along the a direction [Fig. 6(c)]. This magnetic evolution is originated from the strengthened hybridization between As-3*p* and Fe-3*d* orbitals (see Fig. S9 in the Supplemental Material [38] for more detail discussions). The strain-tunable behavior of magnetic coupling is crucial for practical electromechanical nanodevice applications. For example, t-FeAs can be tailored to represent the logic state as either 1 with the FM state or 0 with the AFM state, enabling the attainment of a spin switch. On the other hand, we find that MAE change caused by strain is tunable. A moderate tensile strain for both biaxial and uniaxial tensile strain applied along the short axial direction will change the orientation of the easy axis from the out-of-plane to the in-plane uniaxial direction [Figs. 6(d)–6(f)]. This strain-tunable MAE can be understood based on the second-order perturbation theory (see Fig. S10 in the Supplemental Material [38] for more detail discussions). The robust uniaxial magnetic anisotropy, mainly benefiting from its strain-unbroken structural anisotropy, maintains the long-range ordered low-temperature phase.

B. Effect of U on magnetism of t-FeAs

Figure 7 shows the calculated total magnetic moment per Fe atom of t-FeAs using the GGA + U method with U_{eff} varied from 0 to 5 eV. The magnetic moment increases sharply with increasing U_{eff} until it reaches $2.97 \mu_B$ at $U_{\text{eff}} = 2$ eV. This rather sensitive behavior is reasonable and expected, as that increasing U_{eff} enhances the electron localization. Beyond this critical point, if we continue to increase U_{eff} , the curve becomes flat, and the magnetic moment tends to get saturated, with the saturated magnitude reaching $\sim 3.08 \mu_B$. Consistent with GGA + U ($U_{\text{eff}} = 2 - 5$ eV), the HSE06 functional shows a magnetic moment of $3.13 \mu_B$. In addition,

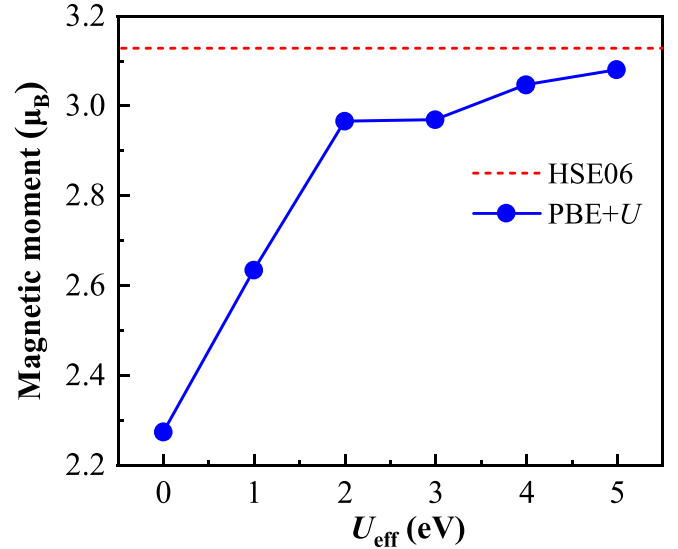


FIG. 7. Magnetic moment per Fe atom of t-FeAs calculated with the HSE06 (dashed line) and GGA + U (solid line) functionals, where U_{eff} is varied from 0 to 5 eV.

we have verified that our qualitative results are reasonable for $U_{\text{eff}} = 2 - 5$ eV. Therefore, $U_{\text{eff}} = 3$ eV is used throughout the paper.

C. Discussion about our results

Before concluding, it is necessary to point out the following: (i) We highlight, as far as we know, that a tunable structural chiral-like atom deviation-nondeviation phase transition is discovered in a 2D system. A strong magnetoelastic coupling in a FM/FEL multiferroic with robust uniaxial magnetic anisotropy is also realized. These two orders are significantly linked to the FEL phase transition and could be directly probed by STM. (ii) Things will be different if we choose the NEB method to search the switching pathway between the initial and final states. Although an energy profile like the normal phase can be observed, a twist one and hence a structural phase transition often goes unrecognized. This indicates that the NEB method acts as an upper limit, as unknown pathways may exist with structural forms of even lower energy. (iii) Our four-state mapping analysis shows that MR-FeAs exhibits AFM coupling, consistent with Ref. [42]. The remaining three polymorphs of monolayer FeAs are found not to exhibit FEL. As previously reported, RuSb, FeSb, CrN, VP, and VAs have the same crystal structure and internal atomic positions as t-FeAs, which are all FM-FEL multiferroic [25,27,69]. Our test calculations show that no analogous elastic strain-induced structural phase transition is observed (Fig. S11 in the Supplemental Material [38]), indicating the role of composition in driving strain-induced structural phase transition. (iv) Although, here, we provide a stable multifunctional 2D material, it is metallic. Atomic monolayer magnetic materials with unique band structure, such as semiconductority, half-metallicity, and topological Dirac states [18,69–71], are usually preferred for future high-performance multifunctional devices such as tunneling magnetoresistance sensors, magnetic random-access memories, and quantum

computation/communication. The hunt for such 2D materials is still on.

VII. CONCLUSIONS

Based on first-principles calculations and MC simulations, we present a 2D t-FeAs monolayer with a rectangular lattice and large perpendicular magnetic anisotropy. Both phonon spectrum calculation and AIMD simulation indicate that t-FeAs is dynamically and thermally stable. We point out that the four-magnetic-configurations method has obvious limits in deriving T_c for a 2D material that possesses a rectangular spin lattice. By employing the four-state mapping analysis, the proposed t-FeAs is identified as an intrinsic FM with high Curie temperature > 435 K. Both T_c and the easy axis of t-FeAs are strain tunable. More importantly, we report a strain-mediated chiral-like atomic distortion behavior. Detailed analysis on the structure and magnetization let us propose that their coupling based on FEL switching could

be directly probed, such as by STM. These highly nontrivial properties endow t-FeAs great potential for applications in sensing and information storage devices and provide opportunities and a platform to explore unprecedented coupling physics beyond the current ones in multiferroic materials.

ACKNOWLEDGMENTS

This paper is partially supported by Fundamental Research Funds for the Central Universities (Grant No. SWU-KR22030), by the National Natural Science Foundation of China (Grant No. 12104294), by the Basic Scientific Research Expenses Program of Universities directly under Inner Mongolia Autonomous Region (Grant No. JY20220213), by Research Program of Science and Technology at Universities of Inner Mongolia Autonomous Region (Grant No. NJZY22389), and calculations were performed in Shanxi Supercomputing Center of China.

Authors declare no competing interests.

-
- [1] A. Soumyanarayanan, N. Reyren, A. Fert, and C. Panagopoulos, Emergent phenomena induced by spin-orbit coupling at surfaces and interfaces, *Nature (London)* **539**, 509 (2016).
- [2] B. Huang, G. Clark, E. Navarro-Moratalla, D. R. Klein, R. Cheng, K. L. Seyler, D. Zhong, E. Schmidgall, M. A. McGuire, D. H. Cobden *et al.*, Layer-dependent ferromagnetism in a van der Waals crystal down to the monolayer limit, *Nature (London)* **546**, 270 (2017).
- [3] M. Bonilla, S. Kolekar, Y. Ma, H. C. Diaz, V. Kalappattil, R. Das, T. Eggers, H. R. Gutierrez, M.-H. Phan, and M. Batzill, Strong room-temperature ferromagnetism in VSe₂ monolayers on van der Waals substrates, *Nat. Nanotechnol.* **13**, 289 (2018).
- [4] Y. Liu, H. Lv, B. Yuan, Y. Liu, Y. Guo, Y. Lin, X. Tai, Y. Qin, J. Peng, J. Zhao *et al.*, Room-temperature long-range ferromagnetic order in a confined molecular monolayer, *Nat. Phys.* **20**, 281 (2024).
- [5] Y. Chen, Q. Fan, Y. Liu, and G. Yao, Electrically tunable magnetism and unique intralayer charge transfer in Janus monolayer MnSSe for spintronics applications, *Phys. Rev. B* **105**, 195410 (2022).
- [6] C. Tang and A. Du, Perspective on computational design of two-dimensional materials with robust multiferroic coupling, *Appl. Phys. Lett.* **122**, 130502 (2023).
- [7] C. Liu, R. Gao, X. Cheng, X. Yang, G. Qin, H. Gao, S. Picozzi, and W. Ren, First-principles study of ferroelectricity, antiferroelectricity, and ferroelasticity in two-dimensional γ -AlOOH, *Phys. Rev. B* **107**, L121402 (2023).
- [8] Y. Gao, M. Gao, and Y. Lu, Two-dimensional multiferroics, *Nanoscale* **13**, 19324 (2021).
- [9] X. Shen, F. Wang, X. Lu, and J. Zhang, Two-dimensional multiferroics with intrinsic magnetoelectric coupling in A-site ordered perovskite monolayers, *Nano Lett.* **23**, 735 (2023).
- [10] C. Wang, X. Ke, J. Wang, R. Liang, Z. Luo, Y. Tian, D. Yi, Q. Zhang, J. Wang, X. F. Han *et al.*, Ferroelastic switching in a layered-perovskite thin film, *Nat. Commun.* **7**, 10636 (2016).
- [11] M. Wu and X. C. Zeng, Intrinsic ferroelasticity and/or multiferroicity in two-dimensional phosphorene and phosphorene analogues, *Nano Lett.* **16**, 3236 (2016).
- [12] Z. Tu and M. Wu, Ultrahigh-strain ferroelasticity in two-dimensional honeycomb monolayers: From covalent to metallic bonding, *Sci. Bull.* **65**, 147 (2020).
- [13] H. Wang and X. Qian, Two-dimensional multiferroics in monolayer group IV monochalcogenides, *2D Mater.* **4**, 015042 (2017).
- [14] W. Li and J. Li, Ferroelasticity and domain physics in two-dimensional transition metal dichalcogenide monolayers, *Nat. Commun.* **7**, 10843 (2016).
- [15] C. Xu, J. Mao, X. Guo, S. Yan, Y. Chen, T. W. Lo, C. Chen, D. Lei, X. Luo, J. Hao *et al.*, Two-dimensional ferroelasticity in van der Waals β' -In₂Se₃, *Nat. Commun.* **12**, 3665 (2021).
- [16] Y. Hu, L. You, B. Xu, T. Li, S. A. Morris, Y. Li, Y. Zhang, X. Wang, P. S. Lee, H. J. Fan *et al.*, Ferroelastic-switching-driven large shear strain and piezoelectricity in a hybrid ferroelectric, *Nat. Mater.* **20**, 612 (2021).
- [17] L. Seixas, A. S. Rodin, A. Carvalho, and A. H. C. Neto, Multiferroic two-dimensional materials, *Phys. Rev. Lett.* **116**, 206803 (2016).
- [18] M.-H. Zhang, X.-L. Chen, W.-X. Ji, P.-J. Wang, Y. Min, and C.-W. Zhang, Discovery of multiferroics with tunable magnetism in two-dimensional lead oxide, *Appl. Phys. Lett.* **116**, 172105 (2020).
- [19] A. Avsar, A. Ciarrocchi, M. Pizzochero, D. Unuchek, O. V. Yazyev, and A. Kis, Defect induced, layer-modulated magnetism in ultrathin metallic PtSe₂, *Nat. Nanotechnol.* **14**, 674 (2019).
- [20] Y. Wang, Y. Huang, Y. Song, X. Zhang, Y. Ma, J. Liang, and Y. Chen, Room-temperature ferromagnetism of graphene, *Nano Lett.* **9**, 220 (2009).
- [21] K. Zhang, L. Wang, and X. Wu, Spin polarization and tunable valley degeneracy in a MoS₂ monolayer via proximity coupling to a Cr₂O₃ substrate, *Nanoscale* **11**, 19536 (2019).
- [22] Z. Wang, C. Tang, R. Sachs, Y. Barlas, and J. Shi, Proximity-induced ferromagnetism in graphene revealed by the anomalous Hall effect, *Phys. Rev. Lett.* **114**, 016603 (2015).
- [23] C. Zhang, Y. Nie, S. Sanvito, and A. Du, First-principles prediction of a room-temperature ferromagnetic Janus VSSe

- monolayer with piezoelectricity, ferroelasticity, and large valley polarization, *Nano Lett.* **19**, 1366 (2019).
- [24] Y. Gao, M. Wu, and X. C. Zeng, Phase transitions and ferroelasticity-multiferroicity in bulk and two-dimensional silver and copper monohalides, *Nanoscale Horiz.* **4**, 1106 (2019).
- [25] X. Xuan, W. Guo, and Z. Zhang, Ferroelasticity in two-dimensional tetragonal materials, *Phys. Rev. Lett.* **129**, 047602 (2022).
- [26] B. Xu, S. Li, K. Jiang, J. Yin, Z. Liu, Y. Cheng, and W. Zhong, Switching of the magnetic anisotropy via strain in two dimensional multiferroic materials: CrSX ($X = \text{Cl, Br, I}$), *Appl. Phys. Lett.* **116**, 052403 (2020).
- [27] X. Cheng, S. Xu, F. Jia, G. Zhao, M. Hu, W. Wu, and W. Ren, Intrinsic ferromagnetism with high Curie temperature and strong anisotropy in a ferroelastic VX monolayer ($X = \text{P, As}$), *Phys. Rev. B* **104**, 104417 (2021).
- [28] Y. Qu, Y. Liao, J. He, Y. Chen, and G. Yao, High-temperature intrinsic two-dimensional-XY ferromagnetism and strong magnetoelastic coupling in tetragonal monolayer MnGe, *J. Phys. Chem. C* **128**, 4631 (2024).
- [29] P. E. Blöchl, Projector augmented-wave method, *Phys. Rev. B* **50**, 17953 (1994).
- [30] G. Kresse and J. Hafner, *Ab initio* molecular dynamics for liquid metals, *Phys. Rev. B* **47**, 558 (1993).
- [31] J. P. Perdew, K. Burke, and M. Ernzerhof, Generalized gradient approximation made simple, *Phys. Rev. Lett.* **77**, 3865 (1996).
- [32] G. Henkelman, B. P. Uberuaga, and H. Jónsson, A climbing image nudged elastic band method for finding saddle points and minimum energy paths, *J. Chem. Phys.* **113**, 9901 (2000).
- [33] A. Togo and I. Tanaka, First principles phonon calculations in materials science, *Scr. Mater.* **108**, 1 (2015).
- [34] M. Di Ventura and S. T. Pantelides, Scanning-tunneling-microscopy images: A fully *ab initio* approach, *Phys. Rev. B* **59**, R5320 (1999).
- [35] K. Momma and F. Izumi, VESTA 3 for three-dimensional visualization of crystal, volumetric and morphology data, *J. Appl. Crystallogr.* **44**, 1272 (2011).
- [36] G. Yao, M.-C. Duan, N. Liu, Y. Wu, D.-D. Guan, S. Wang, H. Zheng, Y.-Y. Li, C. Liu, and J.-F. Jia, Diamagnetic response of potassium-adsorbed multilayer FeSe film, *Phys. Rev. Lett.* **123**, 257001 (2019).
- [37] Q.-Y. Wang, Z. Li, W.-H. Zhang, Z.-C. Zhang, J.-S. Zhang, W. Li, H. Ding, Y.-B. Ou, P. Deng, K. Chang *et al.*, Interface-induced high-temperature superconductivity in single unit-cell FeSe films on SrTiO₃, *Chin. Phys. Lett.* **29**, 037402 (2012).
- [38] See Supplemental Material at <http://link.aps.org/supplemental/10.1103/PhysRevB.110.085432> for details on the exfoliation energy, stabilities, different phases of FeAs, calculated Curie temperature, electronic properties, stress-strain curves, elastic strain controllable MAE, and FEL switching energy profile.
- [39] L. Hu, X. Wu, and J. Yang, Mn₂C monolayer: A 2D antiferromagnetic metal with high Néel temperature and large spin-orbit coupling, *Nanoscale* **8**, 12939 (2016).
- [40] J. He, P. Lyu, and P. Nachtigall, New two-dimensional Mn-based MXenes with room-temperature ferromagnetism and half-metallicity, *J. Mater. Chem. C* **4**, 11143 (2016).
- [41] G. Gao, G. Ding, J. Li, K. Yao, M. Wu, and M. Qian, Monolayer MXenes: Promising half-metals and spin gapless semiconductors, *Nanoscale* **8**, 8986 (2016).
- [42] R. Friedrich, M. Ghorbani-Asl, S. Curtarolo, and A. V. Krashennnikov, Data-driven quest for two-dimensional non-van der Waals Materials, *Nano Lett.* **22**, 989 (2022).
- [43] X. Xuan, T. Yang, J. Zhou, Z. Zhang, and W. Guo, A multiferroic iron arsenide monolayer, *Nanoscale Adv.* **4**, 1324 (2022).
- [44] Y. Jiao, W. Wu, F. Ma, Z.-M. Yu, Y. Lu, X.-L. Sheng, Y. Zhang, and S. A. Yang, Room temperature ferromagnetism and antiferromagnetism in two-dimensional iron arsenides, *Nanoscale* **11**, 16508 (2019).
- [45] L.-M. Yang, V. Bačić, I. A. Popov, A. I. Boldyrev, T. Heine, T. Frauenheim, and E. Ganz, Two-dimensional Cu₂Si monolayer with planar hexacoordinate copper and silicon bonding, *J. Am. Chem. Soc.* **137**, 2757 (2015).
- [46] L.-M. Yang, I. A. Popov, A. I. Boldyrev, T. Heine, T. Frauenheim, and E. Ganz, Post-anti-van't Hoff-Le Bel Motif in atomically thin germanium-copper alloy film, *Phys. Chem. Chem. Phys.* **17**, 17545 (2015).
- [47] N. Sivasdas, M. W. Daniels, R. H. Swendsen, S. Okamoto, and D. Xiao, Magnetic ground state of semiconducting transition-metal trichalcogenide monolayers, *Phys. Rev. B* **91**, 235425 (2015).
- [48] R. Xiao, Z. Guan, D. Feng, and C. Song, Strain-tunable ferromagnetism and skyrmions in two-dimensional Janus Cr₂XYTe₆ ($X, Y = \text{Si, Ge, Sn}$, and $X \neq Y$) monolayers, *J. Appl. Phys.* **135**, 043901 (2024).
- [49] J.-W. Li, Z. Zhang, J.-Y. You, B. Gu, and G. Su, Two-dimensional Heisenberg model with material-dependent superexchange interactions, *Phys. Rev. B* **107**, 224411 (2023).
- [50] N. D. Mermin and H. Wagner, Absence of ferromagnetism or antiferromagnetism in one- or two-dimensional isotropic Heisenberg models, *Phys. Rev. Lett.* **17**, 1133 (1966).
- [51] G. H. O. Daalderop, P. J. Kelly, and M. F. H. Schuurmans, First-principles calculation of the magnetocrystalline anisotropy energy of iron, cobalt, and nickel, *Phys. Rev. B* **41**, 11919 (1990).
- [52] G. H. O. Daalderop, P. J. Kelly, M. F. H. Schuurmans, and H. J. F. Jansen, Magnetic anisotropy in Fe, Co and Ni, *J. Phys. Colloq.* **49**, C8 (1988).
- [53] H. J. Xiang, E. J. Kan, S.-H. Wei, M. H. Whangbo, and X. G. Gong, Predicting the spin-lattice order of frustrated systems from first principles, *Phys. Rev. B* **84**, 224429 (2011).
- [54] H. Xiang, C. Lee, H.-J. Koo, X. Gong, and M.-H. Whangbo, Magnetic properties and energy-mapping analysis, *Dalton Trans.* **42**, 823 (2013).
- [55] P. W. Anderson, Antiferromagnetism. Theory of superexchange interaction, *Phys. Rev.* **79**, 350 (1950).
- [56] J. B. Goodenough, Theory of the role of covalence in the perovskite-type manganites [La, M (II)] MnO₃, *Phys. Rev.* **100**, 564 (1955).
- [57] J. Kanamori, Superexchange interaction and symmetry properties of electron orbitals, *J. Phys. Chem. Solids* **10**, 87 (1959).
- [58] H. Wang, F. Fan, S. Zhu, and H. Wu, Doping enhanced ferromagnetism and induced half-metallicity in CrI₃ monolayer, *Europhys. Lett.* **114**, 47001 (2016).
- [59] N. Miao, B. Xu, L. Zhu, J. Zhou, and Z. Sun, 2D intrinsic ferromagnets from van der Waals antiferromagnets, *J. Am. Chem. Soc.* **140**, 2417 (2018).

- [60] H. Wang, X. Li, J. Sun, Z. Liu, and J. Yang, BP₅ monolayer with multiferroicity and negative Poisson's ratio: A prediction by global optimization method, *2D Mater.* **4**, 045020 (2017).
- [61] T. Zhang, Y. Ma, L. Yu, B. Huang, and Y. Dai, Direction-control of anisotropic electronic behaviors via ferroelasticity in two-dimensional α -MPI ($M = \text{Zr, Hf}$), *Mater. Horiz.* **6**, 1930 (2019).
- [62] D.-s. Wang, R. Wu, and A. J. Freeman, First-principles theory of surface magnetocrystalline anisotropy and the diatomic-pair model, *Phys. Rev. B* **47**, 14932 (1993).
- [63] J. Hu and R. Wu, Giant magnetic anisotropy of transition-metal dimers on defected graphene, *Nano Lett.* **14**, 1853 (2014).
- [64] R. Li, J. Jiang, X. Shi, W. Mi, and H. Bai, Two-dimensional Janus FeXY ($X, Y = \text{Cl, Br, and I}, X \neq Y$) monolayers: Half-metallic ferromagnets with tunable magnetic properties under strain, *ACS Appl. Mater.* **13**, 38897 (2021).
- [65] X. Zhang, L. Wang, H. Su, X. Xia, C. Liu, B. Lyu, J. Lin, M. Huang, Y. Cheng, J.-W. Mei *et al.*, Strain tunability of perpendicular magnetic anisotropy in van der Waals ferromagnets VI₃, *Nano Lett.* **22**, 9891 (2022).
- [66] L. Webster and J.-A. Yan, Strain-tunable magnetic anisotropy in monolayer CrCl₃, CrBr₃, and CrI₃, *Phys. Rev. B* **98**, 144411 (2018).
- [67] C. Huang, J. Feng, F. Wu, D. Ahmed, B. Huang, H. Xiang, K. Deng, and E. Kan, Toward intrinsic room-temperature ferromagnetism in two-dimensional semiconductors, *J. Am. Chem. Soc.* **140**, 11519 (2018).
- [68] D. V. Christensen, Y. Frenkel, Y. Z. Chen, Y. W. Xie, Z. Y. Chen, Y. Hikita, A. Smith, L. Klein, H. Y. Hwang, N. Pryds *et al.*, Strain-tunable magnetism at oxide domain walls, *Nat. Phys.* **15**, 269 (2018).
- [69] X. Xuan, M. Wu, Z. Zhang, and W. Guo, A multiferroic vanadium phosphide monolayer with ferromagnetic half-metallicity and topological Dirac states, *Nanoscale Horiz.* **7**, 192 (2022).
- [70] A. A. Burkov, Topological semimetals, *Nat. Mater.* **15**, 1145 (2016).
- [71] K. F. Mak, J. Shan, and D. C. Ralph, Probing and controlling magnetic states in 2D layered magnetic materials, *Nat. Rev. Phys.* **1**, 646 (2019).